

QCD modeling of hadron physics

P. Maris^{a,b} and P.C. Tandy^b

^aDept. of Physics and Astronomy, University of Pittsburgh, Pittsburgh, PA 15260

^bCenter for Nuclear Research, Dept. of Physics, Kent State University, Kent OH 44242

We review recent developments in the understanding of meson properties as solutions of the Bethe–Salpeter equation in rainbow-ladder truncation. Included are recent results for the pseudoscalar and vector meson masses and leptonic decay constants, ranging from pions up to $c\bar{c}$ bound states; extrapolation to $b\bar{b}$ states is explored. We also present a new and improved calculation of $F_\pi(Q^2)$ and an analysis of the $\pi\gamma\gamma$ transition form factor for both $\pi(140)$ and $\pi(1330)$. Lattice-QCD results for propagators and the quark-gluon vertex are analyzed, and the effects of quark-gluon vertex dressing and the three-gluon coupling upon meson masses are considered.

1. DYSON–SCHWINGER EQUATIONS OF QCD

The Dyson–Schwinger equations [DSEs] are the equations of motion of a quantum field theory. They form an infinite hierarchy of coupled integral equations for the Green’s functions (n -point functions) of the theory. Bound states (mesons, baryons) appear as poles in the Green’s functions. Thus, a study of the poles in n -point functions using the set of DSEs will tell us something about hadrons. For recent reviews on the DSEs and their use in hadron physics, see Refs. [1,2,3].

1.1. Quark propagator

The exact DSE for the quark propagator is¹

$$S(p)^{-1} = i \not{p} Z_2 + m_q(\mu) Z_4 + Z_1 \int_k g^2 D_{\mu\nu}(q) \gamma_\mu \frac{\lambda^i}{2} S(k) \Gamma_\nu^i(k, p), \quad (1)$$

where $D_{\mu\nu}(q = k - p)$ is the renormalized dressed gluon propagator, and $\Gamma_\nu^i(k, p)$ is the renormalized dressed quark-gluon vertex. The notation \int_k stands for $\int^\Lambda d^4k / (2\pi)^4$. For divergent integrals a translationally invariant regularization is necessary; the regularization scale Λ is to be removed at the end of all calculations, after renormalization, and will be suppressed henceforth.

¹We use Euclidean metric $\{\gamma_\mu, \gamma_\nu\} = 2\delta_{\mu\nu}$, $\gamma_\mu^\dagger = \gamma_\mu$ and $a \cdot b = \sum_{i=1}^4 a_i b_i$.

The solution of Eq. (1) can be written as

$$S(p) = \frac{Z(p^2)}{i \not{p} + M(p^2)}, \quad (2)$$

renormalized according to $S(p)^{-1} = i \not{p} + m(\mu)$ at a sufficiently large spacelike μ^2 , with $m(\mu)$ the current quark mass at the scale μ . Both the propagator, $S(p)$, and the vertex, Γ_μ^i depend on the quark flavor, although we have not indicated this explicitly. The renormalization constants Z_2 and Z_4 depend on the renormalization point and on the regularization mass-scale, but not on flavor: in our analysis we employ a flavor-independent renormalization scheme.

1.2. Mesons

Bound states correspond to poles in n -point functions: for example a meson appears as a pole in the 2-quark, 2-antiquark Green’s function $G^{(4)} = \langle 0 | q_1 q_2 \bar{q}_1 \bar{q}_2 | 0 \rangle$. In the vicinity of a meson, i.e. in the neighborhood of $P^2 = -M^2$ with M being the meson mass, such a Green’s function behaves like

$$G^{(4)} \sim \frac{\chi(p_o, p_i; P) \bar{\chi}(k_i, k_o; P)}{P^2 + M^2}, \quad (3)$$

where P is the total 4-momentum of the meson, p_o and p_i are the momenta of the outgoing quark and incoming quark respectively, and similarly for k_i and k_o . Momentum conservation relates these momenta: $p_o - p_i = P = k_o - k_i$.

The function $\chi(p_o, p_i; P)$ describes the projection of the bound state onto its $q\bar{q}$ Fock-space component² (sometimes referred to as the Bethe-Salpeter [BS] wavefunction, which is different from the light-cone wave function). It satisfies the homogeneous Bethe-Salpeter equation [BSE]

$$\Gamma(p_o, p_i; P) = \int_k K(p_o, p_i; k_o, k_i) \chi(k_o, k_i; P), \quad (4)$$

with Γ the Bethe-Salpeter amplitude [BSA]

$$\Gamma(k_o, k_i; P) = S(k_o)^{-1} \chi(k_o, k_i; P) S(k_i)^{-1}. \quad (5)$$

The kernel K is the $q\bar{q}$ irreducible quark-antiquark scattering kernel. This homogeneous integral equation has solutions at discrete values $P^2 = -M^2$ of the total meson 4-momentum P .

In order to identify the meson mass M from the BSE, Eq. (4), it is convenient to first introduce the linear eigenvalue $\lambda(P^2)$ of the kernel

$$\Gamma(p_o, p_i; P) = \lambda(P^2) \int_k K(p_o, p_i; k_o, k_i) \chi(k_o, k_i; P), \quad (6)$$

which has solutions for all values of P^2 . Since we use a Euclidean metric, we have to analytically continue this eigenvalue equation to the timelike region, i.e. negative values of P^2 , and then find M such that $\lambda(-M^2) = 1$. The corresponding eigenvector $\Gamma(p_o, p_i; P)$ is then a solution of the original BSE, Eq. (4), i.e. it is the BSA of a $q\bar{q}$ bound state. This meson BSA is normalized according to

$$2P_\mu = N_c \frac{\partial}{\partial Q_\mu} \left\{ \int_{k,q} \text{Tr} [\bar{\chi}(k_i, k_o) K(\tilde{k}_o, \tilde{k}_i; \tilde{q}_o, \tilde{q}_i) \chi(q_o, q_i)] + \int_k \text{Tr} [\bar{\Gamma}(k_i, k_o) S(\tilde{k}_o) \Gamma(k_o, k_i) S(\tilde{k}_i)] \right\} \Big|_{Q=P} \quad (7)$$

at $P^2 = -M^2$, with $k_o - k_i = P = q_o - q_i$ and $\tilde{k}_o - \tilde{k}_i = Q = \tilde{q}_o - \tilde{q}_i$.

The properly normalized BSA $\Gamma(p_o, p_i; P)$ [or equivalently, $\chi(p_o, p_i; P)$] completely describes

²Here and subsequently, q refers to dressed quark (quasi-particle) states.

the meson as a $q\bar{q}$ bound state. Different types of mesons, such as pseudoscalar or vector mesons, are characterized by different Dirac structures. The ground state in any particular spin-flavor channel corresponds to the largest eigenvalue λ in that channel being one. The first excited state is determined by the next-largest eigenvalue λ being one, and so on for higher excited states.

2. RAINBOW-LADDER TRUNCATION

A viable truncation of the infinite set of DSEs has to respect relevant (global) symmetries of QCD such as chiral symmetry, Lorentz invariance, and renormalization group invariance. For electromagnetic interactions we also need to respect current conservation. The so-called rainbow-ladder truncation respects these properties. In this truncation, the kernel of the meson BSE is replaced by an (effective) one-gluon exchange

$$K(p_o, p_i; k_o, k_i) \rightarrow -4\pi \alpha(q^2) D_{\mu\nu}^{\text{free}}(q) \frac{\lambda_i}{2} \gamma_\mu \otimes \frac{\lambda_i}{2} \gamma_\nu, \quad (8)$$

where $q = p_o - k_o = p_i - k_i$, and $\alpha(q^2)$ is an effective running coupling. The corresponding truncation of the quark DSE is

$$Z_1 g^2 D_{\mu\nu}(q) \Gamma_\nu^i(k, p) \rightarrow 4\pi \alpha(q^2) D_{\mu\nu}^{\text{free}}(q) \gamma_\nu \frac{\lambda_i}{2}. \quad (9)$$

This truncation is the first term in a systematic expansion [4] of the quark-antiquark scattering kernel K ; asymptotically, it reduces to leading-order perturbation theory. Furthermore, these two truncations are mutually consistent in the sense that the combination produces vector and axial-vector vertices satisfying their respective Ward identities. In the axial case, this ensures that in the chiral limit the ground state pseudoscalar mesons are the massless Goldstone bosons associated with chiral symmetry breaking [5,6]. In the vector case, this ensures, in combination with impulse approximation, electromagnetic current conservation [7]. We will come back to this point later, when we discuss electromagnetic processes.

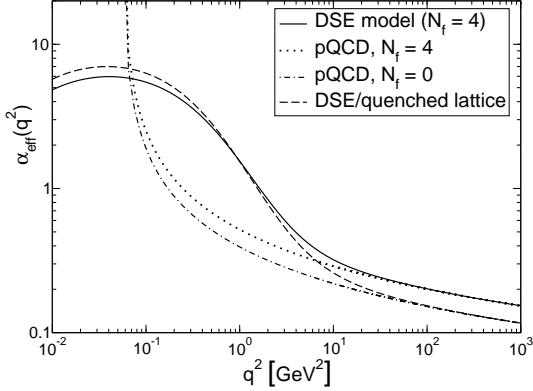


Figure 1. The effective ladder-rainbow kernel from the Maris–Tandy [MT] model [8] compared to LO perturbative QCD and to that deduced from quenched lattice QCD data on the gluon and quark propagators [9].

The ultraviolet behavior of the effective running coupling is dictated by the one-loop renormalization group equation; the infrared behavior of the effective interaction is modeled, and constrained by phenomenology. Here, we are using a 2-parameter model for the effective interaction [8], fitted to give a value for the chiral condensate of $(240 \text{ MeV})^3$ and $f_\pi = 131 \text{ MeV}$. This effective running coupling, with $\Lambda_{\text{QCD}} = 0.234 \text{ GeV}$ and $N_f = 4$, is shown in Fig. 1, and agrees perfectly with pQCD for $q^2 > 25 \text{ GeV}^2$. The model is finite in the infrared region, and it is very similar to an effective interaction that was recently deduced [9] from quenched lattice QCD results for the gluon and quark propagators. Indications are that unquenching does not change the infrared behavior of the running coupling much [10], and thus we believe that this 2-parameter model is a realistic parametrization of the effective quark-quark interaction in the space-like region.

2.1. Quark propagator

A momentum-dependent quark mass function $M(p^2)$ is an essential property of QCD. In the perturbative region this mass function reduces to

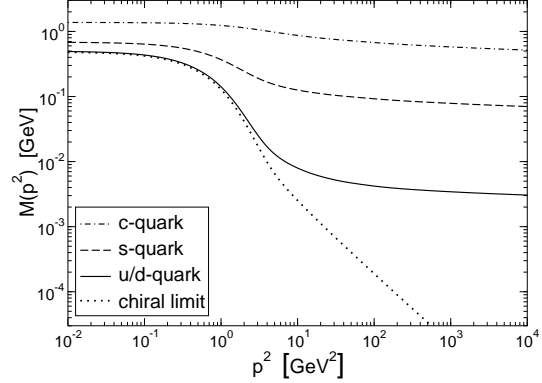


Figure 2. Dynamical quark mass function using the rainbow-ladder truncation of Ref. [8].

the one-loop perturbative running quark mass

$$M(p^2) \simeq \frac{\hat{m}}{\left(\frac{1}{2} \ln \left[p^2/\Lambda_{\text{QCD}}^2\right]\right)^{\gamma_m}}, \quad (10)$$

with $\gamma_m = 12/(33 - 2N_f)$ the anomalous mass dimension. Dynamical chiral symmetry breaking [DχSB] means that this mass function is nonzero even when the current quark mass is zero. In the chiral limit the mass function is [11]

$$M_{\text{chiral}}(p^2) \simeq \frac{2\pi^2\gamma_m}{3} \frac{-\langle\bar{q}q\rangle^0}{p^2 \left(\frac{1}{2} \ln \left[p^2/\Lambda_{\text{QCD}}^2\right]\right)^{1-\gamma_m}}, \quad (11)$$

with $\langle\bar{q}q\rangle^0$ the renormalization-point-independent vacuum quark condensate [6].

It is a longstanding prediction of DSE studies in QCD that both the mass function $M(p^2)$ and the wavefunction renormalisation function $Z(p^2)$ receive strong momentum-dependent corrections at infrared momenta, see e.g. Refs. [1,2,3] and references therein. Provided that the (effective) quark-quark interaction reduces to the perturbative running coupling in the ultraviolet region, it is also straightforward to reproduce the asymptotic behavior of Eqs. (10) and (11) [12,13]. Both these phenomena are illustrated in Fig. 2, using the model for the interaction of Fig. 1. Here we

can also see that in the infrared region the dynamical mass function of the u and d quarks becomes very similar to that of chiral quarks. This is a direct consequence of $D\chi SB$, and leads to a dynamical mass function of several hundred MeV for the light quarks in the infrared region, even though the corresponding current quark masses are only a few MeV. Thus we connect the current quark mass of perturbative QCD with a “constituent-like” quark mass at low energies.

These predictions for the quark mass function have been confirmed in lattice simulations of QCD [14,15,16]. Pointwise agreement for a range of quark masses requires this interaction to be flavor-dependent [9], suggesting that dressing the quark-gluon vertex $\Gamma_\nu^i(q, p)$ is important. The consequences of a dressed vertex for the meson BSEs are currently being explored [17]. This will be discussed in more detail in Sec. 5.

2.2. Pseudoscalar and vector mesons

The most general structure of a pseudoscalar meson BSA is

$$\Gamma^{\text{PS}}(k + \eta P, k - (1 - \eta)P) = \gamma_5 [iE + \not{P} F + \not{k} G + \sigma_{\mu\nu} k_\mu P_\nu H], \quad (12)$$

where the invariant amplitudes E , F , G and H are Lorentz scalar functions of k^2 and $k \cdot P$, and they also depend on the choice for η . The natural choice for mesons with equal-mass constituents (like a pion) is $\eta = \frac{1}{2}$, though physical observables are of course independent of η .

In the chiral limit, the axial-vector Ward–Takahashi identity [WTI] relates the pseudoscalar meson BSA to the (inverse) quark propagator [5]. As a consequence, if there is $D\chi SB$, there is a massless pseudoscalar bound state (Goldstone boson) and vice versa: a massless pseudoscalar bound state indicates that chiral symmetry is broken dynamically. Furthermore, we find

$$E(p^2, p^2) = \frac{M(p^2)}{f_\pi Z(p^2)}. \quad (13)$$

Thus, in the chiral limit we do not have to solve any bound state equation in order to obtain the coefficient function of the canonical Dirac structure of a pseudoscalar meson. This also shows why constituent quark models are inadequate in

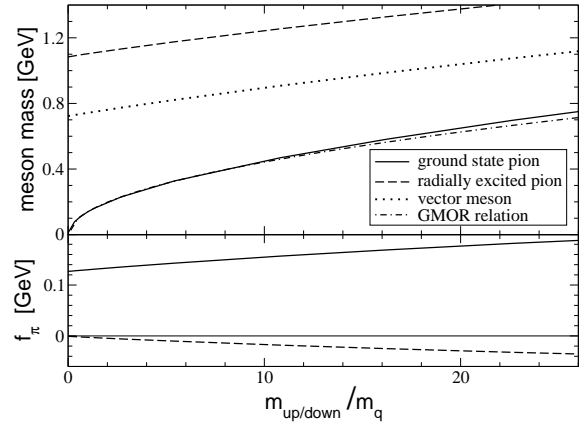


Figure 3. Pion and excited pion mass and decay constant, as function of the current quark mass (normalized by the realistic u/d quark masses); for comparison we have also included the vector meson mass.

describing pions: for a realistic description of pions as $q\bar{q}$ bound states one necessarily has to have a (strongly) momentum dependent quark mass function.

Away from the chiral limit, the axial-vector WTI relates the pseudoscalar and pseudovector spin projections of the BS wavefunction

$$f_{\text{PS}} M_{\text{PS}}^2 = 2 m_q(\mu) r_{\text{PS}}(\mu), \quad (14)$$

where

$$f_{\text{PS}} P_\mu = Z_2 N_c \int_k \text{Tr}[\chi(k_o, k_i) \gamma_5 \gamma_\mu], \quad (15)$$

$$r_{\text{PS}}(\mu) = -i Z_4 N_c \int_k \text{Tr}[\chi(k_o, k_i) \gamma_5]. \quad (16)$$

This is an exact relation in QCD, and holds independent of the current quark mass. The Gell-Mann–Oakes–Renner relation is a direct corollary of this relation, but that is not the only observable consequence. It also means that the decay constant f_{PS} of excited pions vanishes in the chiral limit [18]. This relation is indeed satisfied in the rainbow-ladder truncation, as can be seen from Fig. 3, both for the ground state pion and for its first radial excitation [18]. Furthermore, for

Table 1

DSE results [8] for the meson masses and decay constant, together with experimental data [20].

	experiment (estimates)	calculated ([†] fitted)
$m_{\mu=1\text{GeV}}^{u=d}$	4 - 11 MeV	5.5 MeV
$m_{\mu=1\text{GeV}}^s$	100 - 300 MeV	125 MeV
$-\langle\bar{q}q\rangle_\mu^0$	$(0.24\text{ GeV})^3$	$(0.241^\dagger)^3$
m_π	0.138 GeV	0.138 [†]
f_π	0.131 GeV	0.131 [†]
m_K	0.496 GeV	0.497 [†]
f_K	0.160 GeV	0.155
m_ρ	0.770 GeV	0.742
f_ρ	0.216 GeV	0.207
m_{K^*}	0.892 GeV	0.936
f_{K^*}	0.225 GeV	0.241
m_ϕ	1.020 GeV	1.072
f_ϕ	0.236 GeV	0.259

heavy-light pseudoscalar mesons it predicts [19] that the decay constant decreases like $1/\sqrt{M}$.

The next-lightest mesons are the vector mesons. The BSA of a massive vector meson can be decomposed into eight Dirac structures

$$\Gamma_\mu^V(k + \eta P, k - (1 - \eta)P) = \sum_{i=1}^8 f^i(k^2, k \cdot P; \eta) T_\mu^i(k, P), \quad (17)$$

where $T_\mu^i(k, P)$ are eight independent transverse Dirac tensors. Again, the invariant amplitudes f^i are Lorentz scalar functions of k^2 and $k \cdot P$, and depend on η .

With the model of Ref. [8], we obtain good agreement with the experimental values for the light pseudoscalar and vector meson masses and leptonic decay constants, see Table 1. These results show little sensitivity to variations in the model parameters, as long as the integrated strength of the effective interaction is strong enough to generate an acceptable amount of chiral symmetry breaking, as indicated by the chiral condensate. This is not true for heavier states:

e.g. the radially excited pion is quite sensitive to details of the interaction [21].

2.3. Frame independence

The BSE is usually solved in the rest-frame of the meson. To be explicit, the most convenient frame is that characterized by $P_\mu = (iM, 0, 0, 0)$. However, this is not required: One of the advantages of the DSE approach to hadron physics is its explicit Poincaré covariance. This makes it a particularly useful tool for studying electromagnetic form factors and other processes. No matter what frame one chooses for calculating say the pion electromagnetic form factor, at least one of the pions is moving.

As a test, we have calculated the static π and ρ properties in a moving frame $P_\mu = (iE, q, 0, 0)$ where q is the 3-momentum of the moving meson. Within this frame we solve again the eigenvalue equation, Eq. (6), search for $P^2 = -M^2$ such that $\lambda(P^2) = 1$, and calculate the corresponding electroweak decay constant. Numerically, this is a bit of a tour-de-force, since the Lorentz scalar functions of Eqs. (12) and (17) are now functions of a radial variable k^2 and *two* angles

$$k \cdot P = i k E \cos \alpha + k q \sin \alpha \cos \beta, \quad (18)$$

and the integral equation has to be solved in the three independent variables k^2 , α , and β . With current computer resources, this can be done without further approximations, and the results, shown in Fig. 4, are indeed independent of the meson 3-momentum, illustrating that this approach is indeed Poincaré covariant. We can now use this same approach to calculate meson form factors in an explicitly covariant manner.

3. ELECTROMAGNETIC PROCESSES

In order to study electromagnetic processes, we need to know the dressed quark-photon coupling, in addition to the meson BSAs and the dressed quark propagators.

3.1. Quark-photon vertex

The $q\bar{q}\gamma$ vertex is the solution of the renormalized inhomogeneous BSE with the same kernel K as the homogeneous BSE for meson bound states.

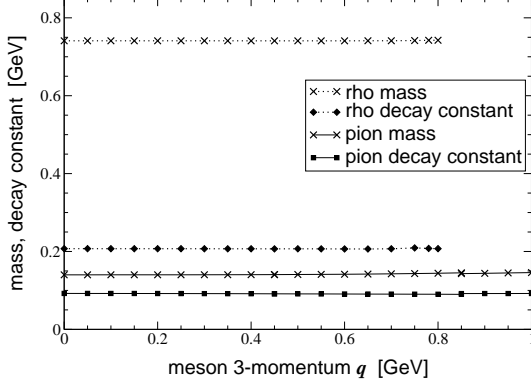


Figure 4. Pion and ρ mass and decay constant calculated in a moving frame, as function of the meson 3-momentum.

That is, for photon momentum Q , we have

$$\Gamma_\mu(p_o, p_i) = Z_2 \gamma_\mu + \int_k K(p_o, p_i; k_o, k_i) \times S(k_o) \Gamma_\mu(k_o, k_i) S(k_i), \quad (19)$$

with p_o and p_i the outgoing and incoming quark momenta, respectively, and similarly for k_o and k_i , with $p_o - p_i = k_o - k_i = Q$. Because of gauge invariance, the vertex satisfies the vector WTI

$$i Q_\mu \Gamma_\mu(p_+, p_-) = S^{-1}(p_+) - S^{-1}(p_-). \quad (20)$$

The most general form of the quark-photon vertex $\Gamma_\mu(p_o, p_i; Q)$ requires a decomposition into twelve Dirac structures. Four of these covariants represent the longitudinal components which are completely specified by the WTI in terms of the (inverse) quark propagator and they do not contribute to elastic form factors. The transverse vertex can be decomposed into eight Dirac tensors $T_\mu^i(p; Q)$ with the corresponding amplitudes being Lorentz scalar functions.

Note that solutions of the *homogeneous* version of Eq. (19) define vector meson bound states with masses $M_V^2 = -Q^2$ at discrete timelike momenta Q^2 . It follows that Γ_μ has poles at those locations and, in the neighborhood of $Q^2 = -M_V^2$, behaves

like [22]

$$\Gamma_\mu(p_o, p_i) \sim \frac{\Gamma_\mu^V(p_o, p_i) f_V M_V}{Q^2 + M_V^2}, \quad (21)$$

where Γ_μ^V is the vector meson BSA, and f_V the electroweak decay constant. The fact that the dressed $q\bar{q}\gamma$ vertex exhibits these vector meson poles lies behind the success of naive vector-meson-dominance [VMD] models; the effects of intermediate vector meson states on electromagnetic processes can be unambiguously incorporated by using the properly dressed $q\bar{q}\gamma$ vertex rather than the bare vertex γ_μ [22].

3.2. Impulse approximation

The generalized impulse approximation allows electromagnetic processes to be described in terms of dressed quark propagators, bound state BSAs, and the dressed $q\bar{q}\gamma$ -vertex. Consider for example the 3-point function describing the coupling of a photon with momentum Q to a pseudoscalar meson $a\bar{b}$, with initial and final momenta $P \pm Q/2$, which can be written as the sum of two terms

$$\Lambda_\mu^{a\bar{b}}(P, Q) = \hat{Q}^a \Lambda_\mu^{aa\bar{b}} + \hat{Q}^{\bar{b}} \Lambda_\mu^{a\bar{b}\bar{b}}, \quad (22)$$

where \hat{Q} is the quark or antiquark electric charge, and where $\Lambda_\mu^{aba}(P, Q)$ and $\Lambda_\mu^{a\bar{b}\bar{b}}(P, Q)$ describe the coupling of a photon to the quark (a) and antiquark (\bar{b}) respectively. In impulse approximation, these couplings are given by

$$\Lambda_\mu^{a\bar{b}}(P, Q) = i N_c \int_k \text{Tr} [\Gamma_\mu^a(q_-, q_+) \chi^{a\bar{b}}(q_+, q) \times S^b(q)^{-1} \bar{\chi}^{\bar{b}a}(q, q_-)], \quad (23)$$

with $q = k - P/2$ and $q_\pm = k + P/2 \pm Q/2$, and similarly for $\Lambda_\mu^{a\bar{b}\bar{b}}$. The corresponding meson elastic form factor is defined by

$$\Lambda_\mu^{a\bar{b}}(P, Q) = 2 P_\mu F(Q^2). \quad (24)$$

3.3. Current conservation

Electromagnetic current conservation dictates $F(0) = \hat{Q}^a + \hat{Q}^{\bar{b}}$ and $Q_\mu \Lambda_\mu^{a\bar{b}}(P, Q) = 0$. It is straightforward to show that both these conditions are satisfied in impulse approximation, in combination with rainbow-ladder truncation. At

$Q = 0$ the $q\bar{q}\gamma$ vertex is completely specified by the differential Ward identity

$$i\Gamma_\mu(p, p) = \frac{\partial}{\partial p_\mu} S^{-1}(p). \quad (25)$$

If this is inserted in Eq. (23), one finds after a change of integration variables

$$\Lambda_\mu^{a\bar{a}b}(P, 0) = 2P_\mu F^{a\bar{a}b}(0) = N_c \int_q \text{Tr} \left[\Gamma^{a\bar{b}}(q', q) S^b(q) \bar{\Gamma}^{\bar{b}a}(q, q') \frac{\partial S^a(q')}{\partial P_\mu} \right], \quad (26)$$

with $q' = q + P$. Comparing this expression to Eq. (7), we recognize that the requirement $F^{a\bar{a}b}(0) = 1$ follows directly from the canonical normalization condition for $\Gamma^{a\bar{b}}$ provided that (1) the BSE kernel K is independent of the total meson momentum P and (2) the $a\bar{a}\gamma$ vertex satisfies the differential Ward identity [7].

The second constraint, $Q_\mu \Lambda_\mu^{a\bar{a}b}(P, Q) = 0$, is satisfied if the quark-photon vertex satisfies the vector WTI. Inserting Eq. (20) into Eq. (23), we find

$$Q_\mu \Lambda_\mu^{a\bar{a}b}(P, Q) = N_c \int_k \text{Tr} [\chi^{a\bar{b}}(q_+, q) \bar{\Gamma}^{\bar{b}a}(q, q_-)] - N_c \int_k \text{Tr} [\Gamma^{a\bar{b}}(q_+, q) \bar{\chi}^{\bar{b}a}(q, q_-)], \quad (27)$$

which clearly vanishes.

The ladder BSE kernel is indeed independent of the meson momentum P , and with quark propagators dressed in rainbow approximation and the dressed quark-photon vertex calculated in ladder approximation, the both the vector WTI and the differential Ward identity are satisfied [22]; thus impulse approximation for the quark-photon vertex in combination with rainbow-ladder truncation is consistent in the sense that the correct electric charge of the meson is produced independent of the model parameters and the resulting meson electromagnetic current is conserved.

3.4. Pion form factor

For the pion electromagnetic form factor, working in the isospin limit, we have

$$2P_\mu F_\pi(Q^2) = iN_c \int_k \text{Tr} [\chi^\pi(q, q_+) \Gamma_\nu(q_+, q_-) \times \bar{\chi}^\pi(q_-, q) S(q)^{-1}]. \quad (28)$$

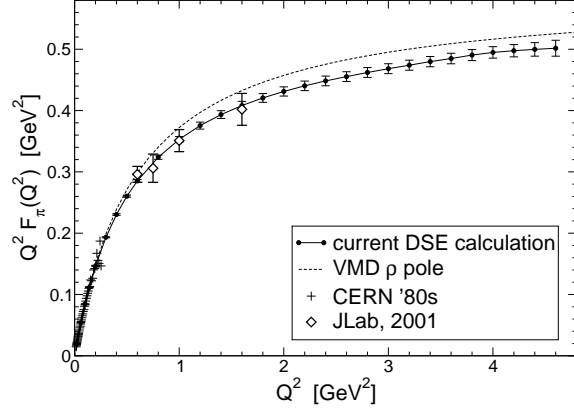


Figure 5. Our results for $Q^2 F_\pi(Q^2)$, with estimates of our numerical error bars, compared to a VMD model and to experimental data from CERN [24] and JLab [25].

with the propagators solutions of the quark DSE in rainbow truncation. The pion BSAs and the $q\bar{q}\gamma$ vertex are solutions of their respective BSEs in ladder truncation, using exactly the same momentum frame as used in the form factor calculation. That does mean re-calculating the pion BSAs for every value of the photon Q^2 , but the advantage is that one does not have to do any interpolation or extrapolation on the numerical solutions of the BSE. Our results for spacelike Q^2 are shown in Fig. 5. They are in excellent agreement with the available experimental data [24,25] and with our previous results³.

Technical difficulties due to the appearance of a pair of complex conjugate singularities in the quark propagator limit our calculation to $Q^2 < 5 \text{ GeV}^2$. Up to this value of Q^2 we see no significant deviation from a naive monopole behavior in our calculation of the form factor. It would be very interesting to see whether or not TJNAF can establish a clear deviation from a monopole behavior, because pQCD predicts a

³The current calculations improve on Refs. [22,23] by eliminating: the Chebyshev expansion for the angular dependence of the restframe BSE solutions, and the interpolation and extrapolation techniques used to connect frames.

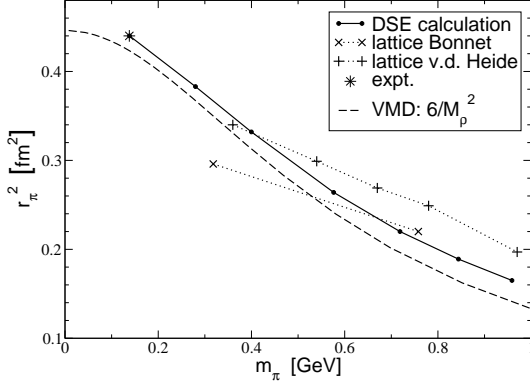


Figure 6. Pion charge radius as function of the quark mass within our DSE model, and as extracted from lattice simulation [26,27].

significantly lower value for $Q^2 F_\pi(Q^2)$ at (asymptotically) large Q^2 .

3.5. Quark mass dependence

We have calculated $F_\pi(Q^2)$ for a range of current quark masses. For all masses considered, the form factor behaves like a monopole, with a monopole mass that is slightly smaller than the ρ -meson mass. A similar behavior has been found in quenched lattice simulations [26,27].

The obtained charge radius, defined by $r^2 = -6F'(0)$, is also in excellent agreement with the experimental value. Our calculated charge radius as a function of the quark mass is shown in Fig. 6, together with the charge radius obtained from lattice simulations. For comparison, we also show the charge radius one would obtain from a naive VMD model, using the corresponding (calculated) vector meson mass. Again, both our numerical result for r_π^2 and that of lattice simulations are represented reasonably well by a VMD model for the charge radius.

An effect that is missing both from our calculations and from quenched lattice simulations are pion loop corrections. At present it is not clear how to incorporate meson loops self-consistently in both the DSE/BSEs and in the approximation for the photon-hadron coupling. However,

in Ref. [28] it was demonstrated that the dressed quark core generates most of the pion charge radius, and that pion loops contribute less than 15% to r_π^2 at the physical value of the pion mass. For larger values of the current quark mass (and thus of the pion mass), we expect these corrections to become negligible. Also for larger spacelike values of Q^2 the effects from meson loops decrease, and for $Q^2 > 1 \text{ GeV}^2$ we expect the contribution of such loops to be negligible.

3.6. $\pi \gamma \gamma$ transition form factor

Using impulse approximation, the coupling of a pion to two photons is, in the isospin limit

$$\Lambda_{\mu\nu}^{\pi\gamma\gamma}(Q_1, Q_2) = \alpha_{\text{em}} \frac{4\pi\sqrt{2}N_c}{3} \int_k \text{Tr}[\chi^\pi(q, p) \Gamma_\mu^\gamma(p, k) S(k) \Gamma_\nu^\gamma(k, q)] , \quad (29)$$

$$= \frac{2i\alpha_{\text{em}}}{\pi} \epsilon_{\mu\nu\alpha\beta} Q_{1\alpha} Q_{2\beta} G_{\pi\gamma\gamma}(Q_1^2, Q_2^2) , \quad (30)$$

where the internal momenta p, q are determined in terms of the integration momentum k and the external momenta Q_1, Q_2 by momentum conservation; furthermore, the pion is on-shell, but the photons not necessarily.

For on-shell photons, $Q_1^2 = 0 = Q_2^2$, the partial decay width $\pi^0 \rightarrow \gamma\gamma$ is given by

$$\Gamma_{\pi\gamma\gamma} = \frac{\alpha_{\text{em}}^2 m_\pi^3}{16\pi^3} G_{\pi\gamma\gamma}^2(0, 0) . \quad (31)$$

This decay width is governed by the axial anomaly as prescribed by electromagnetic current conservations and chiral symmetry. In the chiral limit, the axial anomaly gives⁴

$$G_{\pi\gamma\gamma}(0, 0) = \frac{1}{2\hat{f}_\pi} \approx 5.4 \text{ GeV}^{-1} , \quad (32)$$

and the resulting decay width

$$\Gamma_{\pi\gamma\gamma} = \frac{\alpha_{\text{em}}^2 m_\pi^3}{64\pi^3 \hat{f}_\pi^2} , \quad (33)$$

is within 2% of the experimental width of 7.8 eV. The corrections due to finite pion mass are small.

⁴This expression is conventionally given in terms of $\hat{f}_\pi = f_\pi/\sqrt{2}$, the pion decay constant in the convention where its value is 92 MeV, rather than the convention $f_\pi = 131 \text{ MeV}$ used throughout this work.

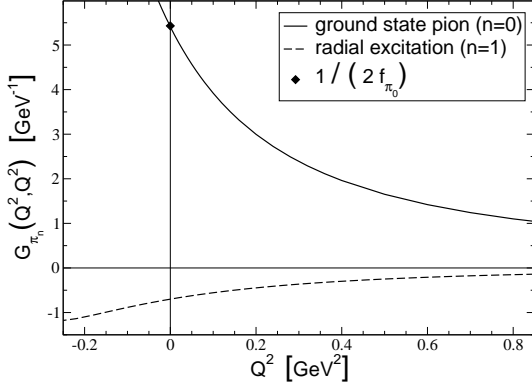


Figure 7. Symmetric $\pi\gamma\gamma$ transition form factor $G(Q^2, Q^2)$ for both the ground state pion and its first radial excitation. Adapted from [21].

The axial anomaly is preserved by the ladder-rainbow truncation of the DSEs combined with an impulse approximation for the $\pi^0\gamma\gamma$ vertex because the relevant manifestations of electromagnetic gauge invariance and chiral symmetry are present [7,29]. We do indeed reproduce the above value for this form factor, as can be seen from Fig. 7. Our results also agree with the experimental data for the transition form factor $G_{\pi^0\gamma^*\gamma}(Q^2, 0)$ [30,31].

On the other hand, the radially excited pion effectively decouples from the axial anomaly [21], and its coupling to two on-shell photons is not constrained by the anomaly. A naive application of Eq. (32) to the first radially excited pion would suggest an enormously large value of 625 GeV^{-1} for its coupling $G(0, 0)$ to two photons, because its decay constant is very small, $\hat{f}_{\pi_1} \approx -0.0016 \text{ GeV}$, and in the chiral limit this decay constant vanishes, as is evident from Eq. (14) and Fig. 3. However, numerically we find that for the excited pion this coupling is about 0.7 GeV^{-1} . Furthermore, the chiral limit $\pi\gamma\gamma$ form factor is at low- Q^2 almost identical to the curves shown in Fig. 7, both for the ground state and for the excited pion.

The asymptotic behavior of this form factor is given by the lightcone operator product expansion [32]

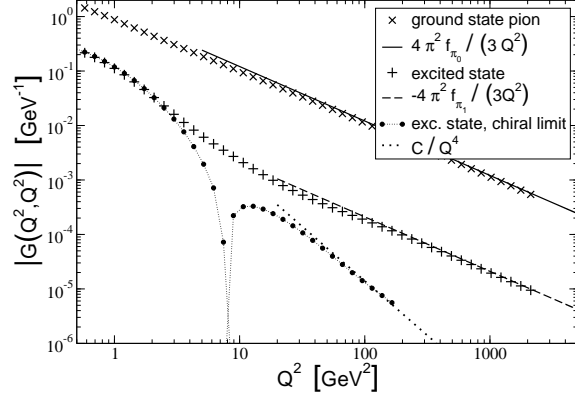


Figure 8. Asymptotic behavior of the symmetric $\pi\gamma\gamma$ transition form factor. Adapted from [21].

sion [32]

$$G(Q_1^2, Q_2^2) \rightarrow 2\pi^2 \hat{f}_{\pi_n} \left\{ \frac{J(\omega)}{Q_1^2 + Q_2^2} + \mathcal{O}\left(\frac{\alpha_s}{\pi}, \frac{1}{(Q_1^2 + Q_2^2)^2}\right) \right\}, \quad (34)$$

where $\omega = (Q_1^2 - Q_2^2)/(Q_1^2 + Q_2^2)$ is the photon asymmetry. In lightfront QCD $J(\omega)$ is related to the leading twist pion distribution amplitude $\phi_\pi(x)$ via

$$J(\omega) = \frac{4}{3} \int_0^1 \frac{dx}{1 - \omega^2(2x - 1)} \phi_\pi(x). \quad (35)$$

The normalization of $\phi_\pi(x)$ immediately gives $J(0) = \frac{4}{3}$ for the case of equal photon virtuality.

Within the present DSE-based approach, it is straightforward to reproduce this leading-order asymptotic behavior analytically, not only for the ground state pion [31], but also for its excited states [21]. Also numerically we reproduce

$$G(Q^2, Q^2) \rightarrow \frac{4\pi^2 \hat{f}_{\pi_n}}{3 Q^2}, \quad (36)$$

as can be seen from Fig. 8.

The interesting question is what happens with the form factor of the (first) radially excited pion in the chiral limit. With a nonzero current

quark mass, this form factor indeed behaves like Eq. (36), and it approaches zero from below as $Q_1^2 = Q_2^2 \rightarrow \infty$, since its decay constant is negative. In the chiral limit however, the decay constant \hat{f}_{π_1} is zero, as dictated by Eq. (14), and evident in Fig. 3. It turns out that in that case the form factor vanishes like $1/Q^4$, with a positive coefficient: the form factor has a zero-crossing in the spacelike region. The coefficient for this $1/Q^4$ behavior depends on the details of the model and its parameters, but it is not simply related to \hat{f}_{π_1} . The leading order behavior of Eq. (36) however is model-independent.

4. MORE MASSIVE MESONS

The rainbow-ladder truncation of the set of DSEs, using the model interaction of Ref. [8], has been very successful in describing a wide range of light meson properties [3]. One question that naturally arises: How does it do for heavier mesons?

4.1. Heavy quark mesons

Let us first address the question of the quark mass dependence of the pseudoscalar and vector meson properties. In Fig. 9 we show the meson mass and decay constants as function of $m_q(19)$, the current quark mass at the renormalization point $\mu = 19$ GeV, both for heavy-light mesons (light meaning u/d quarks and s quarks) and for heavy-heavy mesons.

From this figure it is apparent that all of the meson masses scale approximately linear with the current quark mass above about $m_q \approx 0.5$ GeV $\approx 6m_s$, with m_s being the strange quark mass. The pseudoscalar meson masses show a clear curvature below this mass scale, as one would expect based on the Gell-Mann–Oakes–Renner relation. Also the vector meson masses show a slight curvature at small current quark masses. The results for the D , D_s , η_c , and J/Ψ mesons are in remarkably good agreement with experiments: the calculated masses with $m_c(19) = 0.88$ GeV are within 2% of the experimental values. Compared to the light current quark masses, we find $m_c/m_u = 238$ and $m_c/m_s = 10.5$.

Both the vector and the pseudoscalar masses can be fitted reasonably well over the entire range

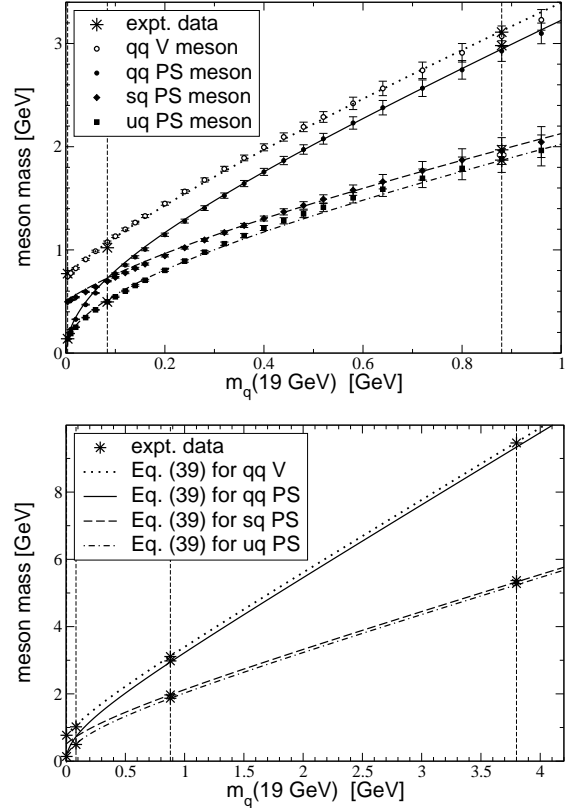


Figure 9. Meson mass as function of m_q . Top: our calculation (with estimates of numerical errors) up to m_c plus the fit Eq. (37); bottom: extrapolated to m_b using the same fit; the vertical dashed lines indicate $m_{u/d}$, m_s , m_c , and m_b .

$0 < m_q < m_c$ by the same formula

$$M^2 = M_0^2 + a_1(m_1 + m_2) + a_2(m_1 + m_2)^2, \quad (37)$$

as indicated by the lines in Fig. 9. Here m_i are the current quark masses of the constituents (at $\mu = 19$ GeV); the chiral limit masses are $M_0^{\text{PS}} = 0$, $M_0^{\text{V}} = 0.75$ GeV; and the remaining fit parameters are $a_1^{\text{PS}} = 2.96$ GeV, $a_1^{\text{V}} = 3.24$ GeV, and $a_2 = 1.12$ both for pseudoscalar and vector mesons.

If we use this fit to extrapolate our results to the bottom quark mass, we get the bottom panel

of Fig. 9. The results for the B , B_s , and Υ mesons are in surprisingly agreement with experiments: the calculated masses with $m_b(19) = 3.8$ GeV are within 1% of the experimental values. Compared to the other current quark masses, we find $m_b/m_c = 4.3$, $m_b/m_s = 45$ and m_b/m_u is about 1,000. Our prediction for η_b is $M_{\eta_b} = 9.34$ GeV

In Fig. 10 shows the corresponding leptonic decay constants. At small current quark masses, all of the decay constants increase with the quark mass, but they tend to level off between the s and the c quark mass, both for the heavy-light and for the heavy-heavy mesons. This is consistent with the expected behavior in the heavy-quark limit: namely a decrease of the decay constant with increasing meson mass (or equivalently, increasing heavy-quark mass) like $f \sim 1/\sqrt{M}$, at least for the heavy-light mesons. Our current calculations suggest that the onset for this asymptotic behavior could be as low as the charm quark mass for the $q\bar{u}$ mesons. However, our results for both f_D and f_{D_s} are about 20% below their experimental values, $f_D = 0.222 \pm 0.020$ GeV [33] and $f_{D_s} = 0.266 \pm 0.032$ GeV [20] respectively, and our result [34] for the decay constant of the J/ψ is about 25% below its experimental value, extracted from the e^+e^- decay [20]. This could indicate that the rainbow-ladder truncation is not reliable in the charm quark region, and/or our model for the effective interaction is not applicable to charm quarks, despite the fact that the meson masses are in good agreement with experiments. Since the decay constants depend on the norm of the BSAs, which in turn depends on the derivative of the quark propagators, it is not a surprise that the decay constants are more sensitive to details of the model than the meson masses, and are thus better indicators for deficiencies in the modeling.

4.2. Heavier u and d quark mesons

Another question is that of heavier states consisting of u and d quarks. Calculations of the a_1 and b_1 mesons using a similar model give results for these masses that are several hundred MeV too low [35,36] when compared to experiments. Also the mass of the first radially excited pion is, within this model, significantly smaller than

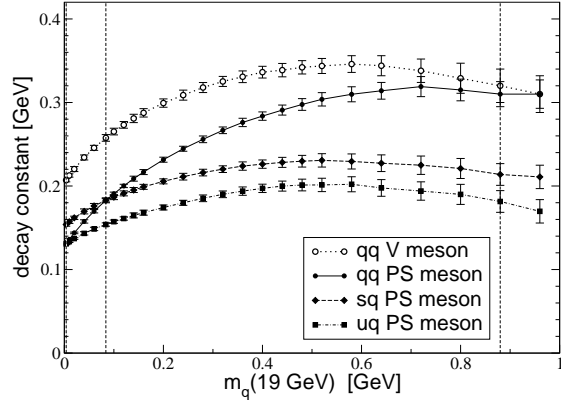


Figure 10. Meson decay constant (with estimates of our numerical errors) as function of m_q , up to the charm quark mass region; the vertical dashed lines indicate $m_{u/d}$, m_s , and m_c .

the experimental value [18]. Furthermore, these heavier mesons, as well as the scalar mesons [37], tend to be more sensitive to details of the interaction than the ρ and π .

This suggests a deficiency of the model and/or of the rainbow-ladder truncation for these higher-mass states. A possible explanation for this deficiency lies in the fact that these higher-mass states have a different spin structure and (especially in case of the radially excited pion) very different BS wave functions, and therefore they are sensitive to different aspects of the BS kernel K . Again, we should study the effects from contributions beyond the rainbow-ladder truncation in more detail in order to resolve these issues.

5. BEYOND THE RAINBOW

Both lattice simulations [38,39] and DSE studies [17,40,41] of the quark-gluon vertex indicate that $\Gamma_\nu^i(q, p)$ deviates significantly from a bare vertex in the nonperturbative region. A (flavor-dependent) nonperturbative vertex dressing could make a significant difference for the solution of the quark DSE [10,17]. Simple dressed vertex models have indicated that material con-

tributions to a number of observables are possible with a better understanding of the infrared structure of the vertex. These diverse model indications include: an enhancement in the quark condensate [10,17]; an increase of about 300 MeV in the b_1/h_1 axial vector meson mass [36]; and about 200 MeV of attraction in the ρ/ω vector meson mass [17].

5.1. Lattice-inspired rainbow model

Over the last five years, the gluon 2-point function has become fairly well known through explicit lattice-QCD calculations [42] and also through approximate solutions of the gauge sector DSEs [2,10,43]. A strictly defined rainbow truncation of the quark DSE for calculation of the dressed quark propagator would proceed from this input. However, the modern information on the dressed gluon propagator shows a strong infrared suppression and it is not possible to obtain a realistic value for the condensate $\langle \bar{q}q \rangle$ in rainbow truncation [44]. In this sense it is clear that the empirically successful rainbow-ladder kernels developed earlier implicitly include effects of quark-gluon vertex dressing for the quark DSE. Although such an effective kernel shows a bare vertex Dirac matrix structure, the infrared parameterization produces a strength and dependence upon gluon momentum that is over and above that of the gluon propagator.

This point is illustrated in Fig. 11 [9], where quenched lattice data on the gluon and quark propagators are used to deduce a phenomenological quark-gluon vertex by means of the DSE. The DSE kernel of Ref. [9] is modeled by $4\pi\alpha(q^2) D_{\mu\nu}^{\text{free}}(q) \rightarrow V(q^2, m_q) D_{\mu\nu}^{\text{lat}}(q)$ in Eq. (9), where $D_{\mu\nu}^{\text{lat}}(q)$ represents the quenched lattice result for the Landau gauge gluon propagator, and $V(q^2, m_q)$ is a phenomenological representation of vertex dressing whose ultraviolet behavior is determined by the requirement that the resulting running coupling reproduces the one-loop renormalization group behavior of QCD. Thus, the vertex dressing has been mapped onto a single amplitude corresponding to the canonical Dirac matrix γ_μ , and depends on the gluon momentum and the current quark mass.

The resulting effective DSE kernel [DSE-Lat] is

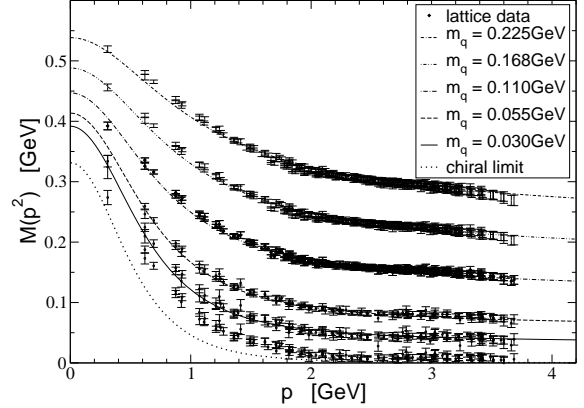


Figure 11. Dynamical quark mass functions obtained with the DSE-Lat model together with the quenched lattice data [15]. Adapted from [9].

compared to the MT model in Fig. 1. The parameters are determined by requiring that the DSE solutions reproduce the quenched lattice data [15] for $S(p)$ in the available domain $p^2 < 10 \text{ GeV}^2$ and $m(\mu = 2 \text{ GeV}) < 200 \text{ MeV}$. In this sense, the DSE-Lat model represents quenched dynamics. It is found that the necessary vertex dressing is a strong but finite enhancement. As one would expect, the vertex dressing $V(q^2, m_q)$ decreases with increasing m_q to represent the effect of quark propagators internal to the vertex.

The model easily reproduces m_π with a current mass that is within acceptable limits. However the resulting chiral condensate $\langle \bar{q}q \rangle = (0.19 \text{ GeV})^3$ is a factor of 2 smaller than the empirical value $(0.24 \pm 0.01 \text{ GeV})^3$. This is attributed to the quenched approximation in the lattice data.

5.2. Modeling the quark-gluon vertex

Let us denote the dressed quark-gluon vertex for gluon momentum k and quark momenta p and $p+k$ by $ig \frac{\lambda_i}{2} \Gamma_\sigma(p+k, p)$. Through $\mathcal{O}(g^2)$, i.e., to one loop, we have $\Gamma_\sigma = Z_{1F} \gamma_\sigma + \Gamma_\sigma^A + \Gamma_\sigma^{\text{NA}}$, see Fig. 12. Here Z_{1F} is the vertex renormalization constant to ensure $\Gamma_\sigma = \gamma_\sigma$ at the renormalization scale μ .

The color factor for Γ_σ^A is $(C_F - \frac{1}{2}C_A) = -\frac{1}{2N_c}$,

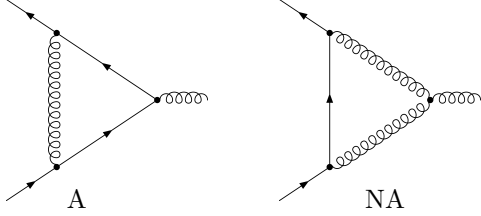


Figure 12. The one-loop corrections to the quark-gluon vertex dressing. Left: the Abelian-like term Γ_σ^A ; Right: the non-Abelian term $\Gamma_\sigma^{\text{NA}}$.

whereas the color factor for $\Gamma_\sigma^{\text{NA}}$ is $\frac{1}{2}C_A = \frac{N_c}{2}$. This reveals two important issues: The Γ_σ^A contribution to the quark-gluon vertex is repulsive, whereas the non-Abelian $\Gamma_\sigma^{\text{NA}}$ term, which involves the three-gluon vertex, is attractive. Furthermore, the magnitude of the non-Abelian term $\Gamma_\sigma^{\text{NA}}$ is enhanced by a factor N_c^2 over the Γ_σ^A term⁵.

The term $\Gamma_\sigma^{\text{NA}}$ involves the triple-gluon vertex $\Gamma_{\mu\nu\sigma}^{3g}$, which is a “new” interaction. However, in Landau gauge the corresponding (bare) Slavnov–Taylor identity reduces $\Gamma_\sigma^{\text{NA}}$ at zero gluon momentum, $k = 0$, to

$$\Gamma_\sigma^{\text{NA}}(p, p) = -i \frac{C_A}{2} \int_q \gamma_\mu S_0(p - q) \gamma_\nu \times \left\{ \frac{\partial}{\partial q_\sigma} g^2 D_0(q^2) \right\} T_{\mu\nu}(q). \quad (38)$$

This expression has been used in a recent model [40] for the dressed quark-gluon vertex at $k = 0$. It is a non-perturbative extension of the two diagrams in Fig. 12. In the ultraviolet, the $\bar{q}q$ scattering kernel appearing in Γ_σ^A coincides with

⁵Note that the color factor of the color-singlet Γ_σ^A contribution to the strong dressing of the quark-photon vertex is $C_F = \frac{N_c^2 - 1}{2N_c}$, i.e. attractive and enhanced by N_c^2 over the color-octet Γ_σ^A term: single gluon exchange between a quark and antiquark has relatively weak repulsion in the color-octet channel, compared to the strong attraction in the color-singlet channel.

the ladder-rainbow kernel; hence the natural extension is $g^2 D_0(q^2) \rightarrow 4\pi\alpha_{\text{eff}}(q^2)/q^2$ and the external quark-gluon vertex is taken to be bare.

For $\Gamma_\sigma^{\text{NA}}$ it takes full advantage of the simplification, Eq. (38), that happens for zero momentum gluons: replace $g^2 D_0(q^2)$ by $4\pi\alpha_{\text{eff}}(q^2)/q^2$. This term is similar to a contribution to the derivative of the quark self-energy but the differences are important; at one-loop this term provides the explicitly non-Abelian contributions to the Slavnov–Taylor identity [45]. The justifications for this nonperturbative vertex model are consistency and simplicity; no new parameters are introduced.

In Fig. 13 we display the results of this model in a dimensionless form for comparison with the (quenched) lattice data for $m(\mu) = 60$ MeV. The general vertex at $k = 0$ has a representation in terms of four invariant amplitudes, but only 3 are non-zero here. We write

$$\Gamma_\sigma(p, p) = \gamma_\sigma \lambda_1(p^2) - 4p_\sigma \gamma \cdot p \lambda_2(p^2) - i2p_\sigma \lambda_3(p^2), \quad (39)$$

since the lattice data [38] are provided in terms of these $\lambda_i(p^2)$ amplitudes. The renormalization scale for both the lattice data and the DSE-Lat model is $\mu = 2$ GeV where $\lambda_1(\mu) = 1$. Without parameter adjustment, the model reproduces the lattice data for λ_1 and λ_3 quite well. The lattice result for λ_2 , despite the large errors, suggests infrared strength that is seriously underestimated by the DSE-Lat model.

The relative contributions to the vertex dressing made by $\Gamma_\sigma^{\text{NA}}$ and Γ_σ^A are indicated by the following amplitude ratios at $p = 0$: $\lambda_1^{\text{NA}}/\lambda_1^A = -60$, $\lambda_2^{\text{NA}}/\lambda_2^A = -14$, and $\lambda_3^{\text{NA}}/\lambda_3^A = -12$. Thus the non-Abelian term $\Gamma_\sigma^{\text{NA}}$ dominates to a greater extent than what the ratio of color factors (-9) would suggest.

Another useful comparison is the corresponding vertex in an Abelian theory like QED; it is given by the differential Ward identity, Eq. (25). With $S^{-1}(p) = i\gamma \cdot p A(p^2) + B(p^2)$, this leads to the correspondance $\lambda_1^{\text{WI}} = A$, $\lambda_2^{\text{WI}} = -A'/2$, and $\lambda_3^{\text{WI}} = B'$, where $f' = \partial f(p^2)/\partial p^2$. The Abelian Ansatz [46], while clearly inadequate for the dominant amplitude λ_1 below 1.5 GeV, does reproduce the DSE-Lat results for both λ_2 and λ_3 .

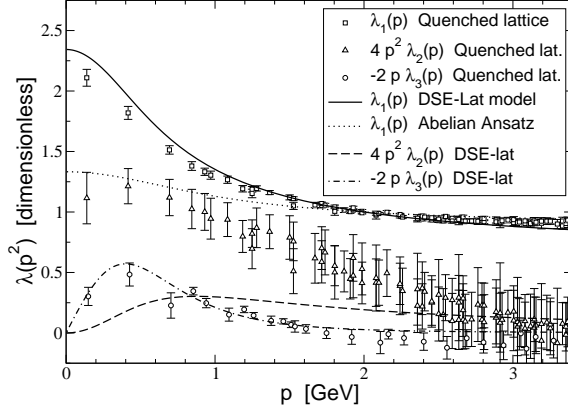


Figure 13. The amplitudes of the dressed quark-gluon vertex at $k = 0$ for $m_q(2 \text{ GeV}) = 60 \text{ MeV}$. Quenched lattice data [38] are compared to the results of the DSE-Lat model [9], and for $\lambda_1(p)$ the Abelian Ansatz is also shown. Adapted from [9].

5.3. Effect on meson observables

There is a known constructive scheme [4] that defines a diagrammatic expansion of the BSE kernel corresponding to any diagrammatic expansion of the quark self-energy such that the vector and axial-vector WTIs are preserved. Among other things, this guarantees the Goldstone boson nature of the flavor non-singlet pseudoscalars independently of model details [5].

This has recently been exploited to produce the first study [17] of how an infinite sub-class of quark-gluon vertex diagrams, including attraction from three-gluon coupling, contributes to vector and pseudoscalar meson masses. The symmetry-preserving BSE kernel obtained from the self-energy has an infinite sub-class of diagrams beyond ladder; it is manageable here because of the algebraic structure afforded from use of a modification of the Munczek-Nemirovsky δ -function model [47]. It is verified that the pseudoscalar $q\bar{q}$ meson remains a Goldstone boson at any order of truncation. As shown in Fig. 14, the ladder-rainbow truncation has at most a 8% repulsive error as m_q is varied up to the b quark region.

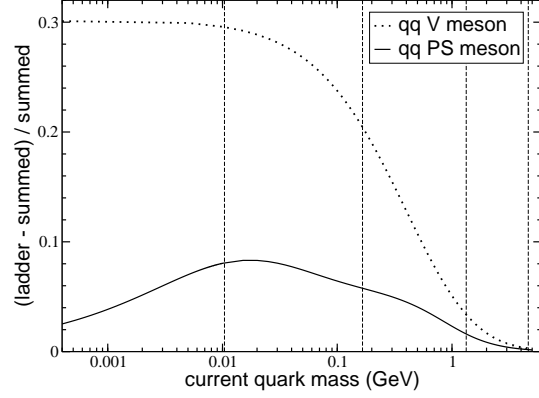


Figure 14. The relative error of the ladder-rainbow truncation relative to the completely resummed model of vertex dressing and corresponding BSE kernel. Adapted from Ref. [17].

Fig. 14 also shows that attraction from the dressed vertex is a significant correction to ladder-rainbow truncation for the $q\bar{q}$ light quark vector mesons, and reduces steadily in relative importance as m_q increases. This is consistent with the results [9] shown in Fig. 11 where the effective vertex dressing $V(q^2, m_q)$ required by quenched lattice-QCD propagators also decreases with (relatively light) m_q . It is also consistent with our results, shown in Fig. 9, for the m_q dependence of the meson masses from the more realistic MT ladder-rainbow model [8]. The reason is that the latter model has a phenomenological infrared strength fitted to empirical light quark information, $\langle \bar{q}q \rangle$; it therefore implicitly includes much of the attraction from vertex dressing. The resulting m_ρ is only 5% off. The algebraic model analysis in Fig. 14 suggests that the relative error of a ladder-rainbow vector mass can only get smaller with increasing m_q ; it should drop by a factor of about 5 in going from the u/d quark region to the c quark region, and be about 1% for b quarks. That is what we find for the MT model in Fig. 9; the error is only 2% for c quarks and 1% for b quarks. Although the algebraic model is simple and not all details will be realistic, we ex-

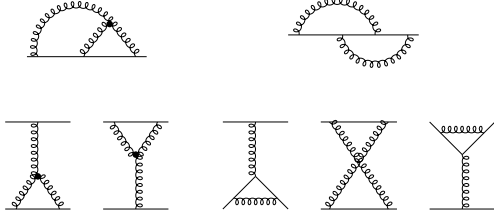


Figure 15. The two leading-order (1-loop) vertex corrections to the rainbow DSE (top) and the corresponding 5 additions to the ladder BSE kernel (bottom) to preserve the relevant Ward identities. Quark and gluon lines are dressed.

pect the qualitative aspects of these observations to be confirmed whenever a more realistic study becomes feasible.

5.4. Current conservation

If one goes beyond the rainbow-ladder truncation for the propagators, the meson BSAs and the quark-photon vertex, one has to go beyond impulse approximation for the meson form factor to ensure current conservation [23]. For example, following the general procedure of Ref. [4], one-loop dressing of the quark-gluon vertex in the DSE requires 5 additions to the ladder BSE kernel to preserve the relevant WTIs, see Fig. 15.

The resulting BSE kernel $K(q_o, q_i; k_o, k_i)$ now becomes dependent on the total meson momentum $P = q_o - q_i = k_o - k_i$, which means that the first term in the normalization condition, Eq.(7), is nonzero. With the choice $k_o = k + P$, $k_i = k$, this introduces the 4 extra terms in the normalization condition depicted in the top row of Fig. 16. These 4 additional diagrams are generated from the BSE kernel in the bottom part of Fig. 15 by taking the derivative with respect to the meson momentum P , where P flows through one quark propagator only. Since a derivative with respect to P is equivalent to the insertion of a zero-momentum photon according to the differential Ward identity, Eq. (25), it is obvious which diagrams have to be added to the impulse approxi-

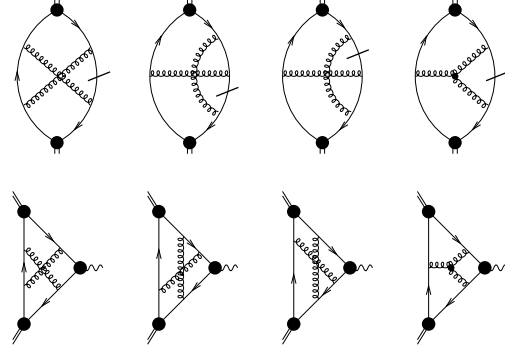


Figure 16. Top: The 4 contributions to the BSA normalization condition from the additions of Fig. 15 to the DSE dynamics. Bottom: The corresponding 4 corrections to the impulse approximation to the form factor. Slashes denote derivatives as described in the text.

mation to maintain current conservation [23], and they are displayed in the bottom row of Fig. 16. The transversality of the photon-meson coupling is also maintained by this truncation.

We note that this procedure systematically exposes Fock-space components of the meson that are included in the exact $q\bar{q}$ scattering kernel of the BSE but which necessarily show up explicitly as corrections to the impulse approximation.

6. CONCLUDING REMARKS

We have shown how the rainbow-ladder truncation of the set of DSEs can be applied to study pseudoscalar and vector meson properties, from pions up to $b\bar{b}$ bound states. This truncation respects the relevant symmetries and related Ward identities: e.g. the axial-vector WTI, which ensures the Goldstone nature of the pions in the chiral limit; we also preserve the correct QCD renormalization properties. Another advantages of this approach is its manifest Poincaré invariance, which makes the study of electromagnetic form factors relatively simple. In addition to the dressed quark propagators and bound state amplitudes, one needs the quark-photon vertex,

which can be obtained by solving an inhomogeneous BSE [22]. The rainbow-ladder truncation, in combination with impulse approximation for the form factor, guarantees current conservation. Our result for $F_\pi(Q^2)$ is in remarkable agreement with the data from TJNAF [25].

The results for the kaon form factors are also in good agreement with the data [23], as are the results for the radiative [30,31] and strong decays [48] of the vector mesons, without any readjustments of the model parameters. Hadronic processes involving four (or more) external particles can also be described in this framework, though one has to go beyond impulse approximation. Our results for π - π scattering [49] agree with predictions from chiral symmetry, and this method has been applied to the anomalous $\gamma\pi\pi\pi$ coupling [50] as well. This approach unambiguously incorporates bound state effects in processes that receive contributions from off-shell intermediate mesons, such as σ and ρ mesons in case of π - π scattering [49], and VMD effects in the case of electromagnetic interactions.

Within the same framework, one can consider baryons as bound states of a quark and a diquark, the latter in a color anti-triplet configuration. It has been shown [51] that one can obtain a reasonable description of the ground state octet and decouplet baryons using both scalar and axial-vector diquarks. There has also been significant progress in understanding the nucleon form factors using this approach [52].

7. ACKNOWLEDGEMENTS

This work was supported by the US Department of Energy, contract No. DE-FG02-00ER41135 and by the National Science Foundation, grant No. PHY-0301190. The work benefited from the facilities of the NSF Terascale Computing System at the Pittsburgh Supercomputing Center. We thank C.D. Roberts for very useful discussions and are grateful to P. Bowman and J.I. Skullerud for providing lattice-QCD results. Appreciation is extended to D. Leinweber, the Light Cone organizing committee, and the staff and members of the CSSM, University of Adelaide for hospitality and support.

REFERENCES

1. C.D. Roberts and A.G. Williams, Prog. Part. Nucl. Phys. **33**, 477 (1994) [arXiv:hep-ph/9403224]; P.C. Tandy, Prog. Part. Nucl. Phys. **39**, 117 (1997) [arXiv:nucl-th/9705018]. C.D. Roberts and S.M. Schmidt, Prog. Part. Nucl. Phys. **45S1**, 1 (2000) [arXiv:nucl-th/0005064].
2. R. Alkofer and L. von Smekal, Phys. Rept. **353**, 281 (2001) [arXiv:hep-ph/0007355].
3. P. Maris and C.D. Roberts, Int. J. Mod. Phys. E **12**, 297 (2003) [arXiv:nucl-th/0301049].
4. A. Bender, C.D. Roberts and L. Von Smekal, Phys. Lett. B **380**, 7 (1996) [arXiv:nucl-th/9602012]; A. Bender, W. Detmold, C.D. Roberts and A.W. Thomas, Phys. Rev. C **65**, 065203 (2002) [arXiv:nucl-th/0202082].
5. P. Maris, C.D. Roberts and P.C. Tandy, Phys. Lett. B **420**, 267 (1998) [arXiv:nucl-th/9707003].
6. P. Maris and C.D. Roberts, Phys. Rev. C **56**, 3369 (1997) [arXiv:nucl-th/9708029].
7. C.D. Roberts, Nucl. Phys. A **605**, 475 (1996) [arXiv:hep-ph/9408233].
8. P. Maris and P.C. Tandy, Phys. Rev. C **60**, 055214 (1999) [arXiv:nucl-th/9905056].
9. M.S. Bhagwat, M.A. Pichowsky, C.D. Roberts and P.C. Tandy, Phys. Rev. C **68**, 015203 (2003) [arXiv:nucl-th/0304003].
10. C.S. Fischer and R. Alkofer, Phys. Rev. D **67**, 094020 (2003) [arXiv:hep-ph/0301094].
11. H.D. Politzer, Nucl. Phys. B **117**, 397 (1976).
12. K. Higashijima, Phys. Rev. D **29**, 1228 (1984).
13. P.I. Fomin, V.P. Gusynin, V.A. Miransky and Y.A. Sitenko, Riv. Nuovo Cim. **6N5**, 1 (1983).
14. J. Skullerud, D.B. Leinweber and A.G. Williams, Phys. Rev. D **64**, 074508 (2001) [arXiv:hep-lat/0102013].
15. P.O. Bowman, U.M. Heller, D.B. Leinweber and A.G. Williams, Nucl. Phys. Proc. Suppl. **119**, 323 (2003) [arXiv:hep-lat/0209129].
16. P.O. Bowman *et al.*, Nucl. Phys. Proc. Suppl. **128** (2004) 23 [arXiv:hep-lat/0403002].
17. M.S. Bhagwat *et al.*, Phys. Rev. C **70**, 035205

- (2004) [arXiv:nucl-th/0403012].
18. A. Holl, A. Krassnigg and C.D. Roberts, Phys. Rev. C **70**, 042203 (2004) [arXiv:nucl-th/0406030].
 19. M.A. Ivanov, Y.L. Kalinovsky, P. Maris and C.D. Roberts, Phys. Rev. C **57**, 1991 (1998) [arXiv:nucl-th/9711023].
 20. S. Eidelman *et al.* [Particle Data Group Collaboration], Phys. Lett. B **592**, 1 (2004)
 21. A. Holl *et al.*, Phys. Rev. C **71**, 065204 (2005) [arXiv:nucl-th/0503043].
 22. P. Maris and P.C. Tandy, Phys. Rev. C **61**, 045202 (2000) [arXiv:nucl-th/9910033].
 23. P. Maris and P.C. Tandy, Phys. Rev. C **62**, 055204 (2000) [arXiv:nucl-th/0005015].
 24. S.R. Amendolia *et al.* [NA7 Collaboration], Nucl. Phys. B **277**, 168 (1986).
 25. J. Volmer *et al.* [The Jefferson Lab F(pi) Collaboration], Phys. Rev. Lett. **86**, 1713 (2001) [arXiv:nucl-ex/0010009].
 26. J. van der Heide, J.H. Koch and E. Laermann, Phys. Rev. D **69**, 094511 (2004) [arXiv:hep-lat/0312023].
 27. F.D.R. Bonnet *et al.* [LHP Collaboration], Phys. Rev. D **72**, 054506 (2005) [arXiv:hep-lat/0411028].
 28. R. Alkofer, A. Bender and C.D. Roberts, Int. J. Mod. Phys. A **10**, 3319 (1995) [arXiv:hep-ph/9312243].
 29. P. Maris and C.D. Roberts, Phys. Rev. C **58**, 3659 (1998) [arXiv:nucl-th/9804062].
 30. P. Maris, Nucl. Phys. Proc. Suppl. **90**, 127 (2000) [arXiv:nucl-th/0008048].
 31. P. Maris and P.C. Tandy, Phys. Rev. C **65**, 045211 (2002) [arXiv:nucl-th/0201017].
 32. G.P. Lepage and S.J. Brodsky, Phys. Rev. D **22**, 2157 (1980); M.K. Chase, Nucl. Phys. B **167**, 125 (1980).
 33. M. Artuso *et al.* [CLEO Collaboration], arXiv:hep-ex/0508057.
 34. A. Krassnigg and P. Maris, J. Phys. Conf. Ser. **9**, 153 (2005) [arXiv:nucl-th/0412058].
 35. R. Alkofer, P. Watson and H. Weigel, Phys. Rev. D **65**, 094026 (2002) [arXiv:hep-ph/0202053].
 36. P. Watson, W. Cassing and P.C. Tandy, Few Body Syst. **35**, 129 (2004) [arXiv:hep-ph/0406340].
 37. P. Maris, Few Body Syst. **32**, 41 (2002) [arXiv:nucl-th/0204020].
 38. J.I. Skullerud *et al.*, JHEP **0304**, 047 (2003) [arXiv:hep-ph/0303176].
 39. J.I. Skullerud *et al.*, Nucl. Phys. Proc. Suppl. **141**, 244 (2005) [arXiv:hep-lat/0408032].
 40. M.S. Bhagwat and P.C. Tandy, Phys. Rev. D **70**, 094039 (2004) [arXiv:hep-ph/0407163].
 41. R. Alkofer, C.S. Fischer and F.J. Llanes-Estrada, Phys. Lett. B **611**, 279 (2005) [arXiv:hep-th/0412330].
 42. D.B. Leinweber, J.I. Skullerud, A.G. Williams and C. Parrinello [UKQCD Collaboration], Phys. Rev. D **60**, 094507 (1999) [Erratum-ibid. D **61**, 079901 (2000)] [arXiv:hep-lat/9811027].
 43. L. von Smekal, R. Alkofer and A. Hauck, Phys. Rev. Lett. **79**, 3591 (1997) [arXiv:hep-ph/9705242]; *ibid.*, Annals Phys. **267**, 1 (1998) [Erratum-ibid. **269**, 182 (1998)] [arXiv:hep-ph/9707327].
 44. F.T. Hawes, P. Maris and C.D. Roberts, Phys. Lett. B **440**, 353 (1998) [arXiv:nucl-th/9807056].
 45. A.I. Davydychev, P. Osland and L. Saks, Phys. Rev. D **63**, 014022 (2001) [arXiv:hep-ph/0008171].
 46. J.S. Ball and T. W. Chiu, Phys. Rev. D **22**, 2542 (1980).
 47. H.J. Munczek and A.M. Nemirovsky, Phys. Rev. D **28** (1983) 181.
 48. D. Jarecke, P. Maris and P.C. Tandy, Phys. Rev. C **67**, 035202 (2003) [arXiv:nucl-th/0208019].
 49. P. Bicudo *et al.*, Phys. Rev. D **65**, 076008 (2002) [arXiv:hep-ph/0112015]; S.R. Cotanch and P. Maris, Phys. Rev. D **66**, 116010 (2002) [arXiv:hep-ph/0210151].
 50. S.R. Cotanch and P. Maris, Phys. Rev. D **68**, 036006 (2003) [arXiv:nucl-th/0308008].
 51. M. Oettel, G. Hellstern, R. Alkofer and H. Reinhardt, Phys. Rev. C **58**, 2459 (1998) [arXiv:nucl-th/9805054].
 52. R. Alkofer *et al.*, Few Body Syst. **37**, 1 (2005) [arXiv:nucl-th/0412046]; A. Holl *et al.*, Nucl. Phys. A **755**, 298 (2005) [arXiv:nucl-th/0501033].